Axial vs Equatorial: Photocrystallographic Investigation of Intramolecular Charge Transfer (ICT) State Geometry in Conformational Polymorphs of a Donor-Bridge-Acceptor System

Krishnayan Basuroy,*[a] Jose de J. Velazquez-Garcia,[a] Darina Storozhuk,[a] Robert Henning,[b] David J. Gosztola,[c] Sreevidya Thekku Veedu[a] and Simone Techert*[a][d]

[a] Deutsches Elektronen-Synchrotron DESY, Notkestr. 85, 22607 Hamburg, Germany. Department
[b] Center for Advanced Radiation Sources, The University of Chicago, Chicago, Illinois 60637, USA
[c] Center for Nanoscale Materials, Argonne National Laboratory, Lemont, Illinois 60439, USA.
[d] Institute of X-ray Physics, University of Göttingen, Friedrich-Hund-Platz 1, 37077 Göttingen, Germany.

Abstract: Two conformational polymorphs of a charge transfer (CT) compound, pyrene-$(CH_2)_2$-*N,N'*-dimethylaniline (PyCHDMA), were investigated. The fluorescence spectra collected in different solvents exhibited evidence of intramolecular CT(ICT). The intra- and inter-fragment charge transfer analysis for the conformers using results from TDDFT calculations show that ICT in the 1st excited state is entirely dominated by electrons transferred from the nitrogen atom in DMA moiety to the pyrene moiety. The photocrystallography data from time-resolved X-ray diffraction (TRXRD) measurements with pink Laue radiation shows larger intramolecular electron transfer (IET) in the 1st excited state (ES), with the shortening of the N-C bond due to a decreased repulsion between the lone-pair and the bond pair in the central nitrogen atom, which further induces the planarity in the C-N-$(CH_3)_2$ moiety, in both the polymorphs. The natural bonding orbital (NBO) analyses further confirm the IET process and also presents the change in partial atomic charges in going from GS and ES, with Hirshfeld partition and natural population analysis (NPA).

Introduction

Photoinduced charge transfer (PCT) reactions are considered essential in many biological and chemical reactions of wide significance, such as natural photosynthesis,[1] repair of DNA lesions,[2] photoelectric conversion in organic solar cells,[3] and photodegradation of pollutants,[4] etc. Especially, the natural photosynthesis process in plants provides an excellent blueprint for an efficient solar energy conversion procedure that may allow us to produce and store energy in a form useful to us.[5] The wide impact of the PCT process has encouraged investigation of the process in various model systems to design highly responsive, fine-tuned optoelectronic smart materials.[6]

While investigating the PCT process in purely organic modeled systems, pyrene-based molecules are considered an attractive choice, owing to their high charge carrier mobility,[7] and long-lived singlet excited states[8]. Pyrene-based charge transfer (CT) molecules are often designed by attaching pyrene to an electron-rich moiety such as *N,N'*-dimethylaniline (DMA), directly or otherwise, to explore the essential aspects of the photoinduced electron transfer (PET) process and intramolecular charge transfer (ICT) states in different donor-acceptor (D-A)[9] or donor-bridge-acceptor (D-B-A)[10] molecular templates, where pyrene acts as an electron acceptor and DMA as a donor. Though most of the spectroscopic and theoretical studies on pyrene-bridge-DMA systems are focused on analyzing the PCT process in solution,[7,9-11] it is the studies in the crystalline state that deems essential to design suitable systems for application in the field of solid-state materials[12]. In this regard, single crystals are considered much more efficient in the conversion of photon energies, especially owing to their lesser defects and grain boundaries.[13] Unfortunately, the structural changes associated with the intramolecular charge transfer (ICT) process in solids for either D-A or D-B-A systems, are not studied much and are not well understood, yet.[14]

The ICT states can be quite different from the ground state (GS) in terms of electronic structure and molecular geometry, provided the molecule is not very rigid.[15] Two models, the "twisted" ICT (TICT)[15][16] state with an axial conformation, and the "planar" ICT (PICT)[17] state with an equatorial conformation, between the D and A-groups, in the respective ICT state geometries, for D-A or D-rigid group-A, were proposed. In the D-B-A system with a flexible bridging group, the charge transfer rate or ICT state geometry of the donor or the acceptor moiety would heavily rely on the conformation of the bridging group.[15] Though pyrene-bridge-DMA systems with flexible $(CH_2)_n$ single-bond connectors germinate uncertainties in the conformation of the molecule, it also provides the potential to have different conformations when single crystals evolve from solutions.[18] At lower-to-ambient temperatures, the reaction in the solid state still holds the "topochemical postulate" relevant and therefore suggests a minimum of atomic or molecular movement during the solid-state reaction.[19] Therefore, it would be interesting to investigate the changes associated with the ICT state geometry of a D-B-A model system in the solid state.

In recent times, time-resolved X-ray diffraction (TRXRD), mostly, time-resolved photocrystallography has evolved as an effective methodology to do the real-time investigation of photo-induced processes in small molecules, in solids.[20] Most of the small molecule systems, studied by TRXRD, are designed to investigate light irradiated transient species in spin-crossover systems,[21] purely organic molecules with weak interactions[22] or metal-to-ligand (MLCT) or ligand-to-metal (LMCT) charge transfer processes, in solids[23]. The examples of even studying purely organic charge transfer molecules by employing TRXRD are also quite rare.[14][24]

In the present study, a mono-substituted pyrene derivative, pyrene-$(CH_2)_2$-*N,N'*-dimethylaniline, PyCHDMA, was designed where dimethylaniline (DMA) is connected to pyrene through an alkane chain, $(CH_2)_2$ (Figure1a), to design an ICT molecule. The electron-rich DMA moiety is acting as an electron donor and the pyrene moiety acts as an electron acceptor. The serendipitous occurrence of two conformational polymorphs[19] for PyCHDMA has provided us the opportunity to do a comparative analysis of the influence of their respective conformations, on the light-driven processes, in single crystals.

Results and Discussion

PyCHDMA crystallized in two polymorphic forms, PyCHDMA1 (space group *P*-1) and PyCHDMA20 (space group $P2_1/n$), in two separate crystallization batches in ethanol/ethyl acetate binary mixtures. Both the molecules are crystallized in centrosymmetric space groups with one molecule in the crystallographic asymmetric unit. While, in the crystal structure of PyCHDMA1, pyrene and dimethylaniline are in axial orientations with an interplanar angle of 72.74°, in PyCHDMA20 they are in equatorial conformation with an interplanar angle of 4.28° (Figures 1b and c). The difference in conformation is quite clearly visible in the superposition diagram of PyCHDMA1 and PyCHDMA20 (Figure 1b). The difference in the conformations between the polymorphs can be defined by a torsion about the single bond defined in Figure 1a. The respective torsion angle values for PyCHDMA1 and PyCHDMA20 are indicated in Figures 1c and d. The extent of overlap between the π-π stacked pyrene moieties in PyCHDMA1 and PyCHDMA20 crystals are ~66% and ~17%, respectively (Figure S8). But, the overlap of the effective van der Waals volume[25] of the π-π stacked molecules is greater in PyCHDMA20 compared to PyCHDMA1. This was also reflected in the energy framework analysis performed with CrystalExplorer 21.5.[26] The energy framework analysis was performed to calculate interaction energies that stabilized the packing of molecules in both the crystals. The interaction energies are calculated using the ground state (GS) geometries obtained from single crystal XRD measurements. The interaction energies between the π-π stacked molecular pairs in PyCHDMA1 and PyCHDMA20 crystals are -62.2 kJ/mol and -71.7 kJ/mol, respectively. In both cases, a major contribution to these energy values is from dispersion interactions (Table S5).

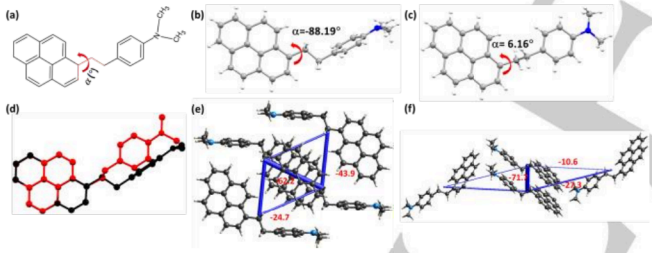

Figure 1. (a) Chemical structure of pyrene-$(CH_2)_2$-*N*,*N*'-dimethylaniline (PyCHDMA). The torsion angle, α, is defined with bonds in red. (b) and (c) are the molecular conformations of PyCHDMA1 and PyCHDMA20, respectively. (d) Superposition of PyCHDMA1(black) and PyCHDMA20 (red), keeping the pyrene moieties overlapped. (e) and (f) Intermolecular interaction energies between different set of dimers, calculated using CrystalExplorer, are provided, for PyCHDMA1 and PyCHDMA20, respectively (thickness of the cylinders are propotional to the strength of interaction, as the associated values in kJ/mol are suggesting).

The absorption and emission spectra of PyCHDMA in three different solvents, toluene, ethyl acetate, and ethanol were collected at different concentrations (Figure S1). The absorption spectra collected with different solvents do not show any difference or change in the relative intensity of vibronic bands, with either the changing solvent polarity or the concentration (Figure S1). The emission spectra collected at the different solvents show a strong presence of dual emission, both from the locally excited (LE) state and the CT state (Figures S1 and S2). While the low wavelength characteristic emission peaks correspond to the radiative transition from the LE state, it is the broad structure less CT band that makes this molecule interesting. The emission maxima of the CT band clearly show the presence of a bathochromic shift while gradually increasing the polarity of the solvents, from toluene to ethyl acetate to ethanol (Figure S2). The solvatochromism observed for the fluorescence spectra clearly indicated the strong ICT nature of PyCHDMA.[29] The observed increment of stokes shift in going from toluene to ethanol is ~60nm (Figure S2), which clearly suggest the strong ICT nature of the molecule.[27]

The difference in the conformations of PyCHDMA1 and PDCHMA20 was investigated with a gas-phase potential energy scan (PES) on the torsion angle, α, at 10° intervals, from -180° to 180°, at the M062X/6-311G**[28]level of theory (Figure 2a). The PES results show that the axial conformation between the two π-rings of pyrene and DMA, in PyCHDMA1, is close to a global minimum with respect to the optimized energy values and therefore can be considered the polymorph representing the stable thermodynamic form.[29] Whereas, the equatorial conformation between pyrene and DMA in PyCHDMA20 was close to a local minimum (Figure 2a) and can be considered as the polymorphic representation of the metastable kinetic form.[29] Figure 2a shows that in order to go from the molecular conformation of PyCHDMA1 to the conformation of PyCHDMA20, a potential barrier of the height > 2kcal/mol needs to be crossed by rotation about a single bond, suggesting the nature of the polymorphs is conformational.[18] The charge transfer characteristics of PyCHDMA1 and PyCHDMA20 monomers with their specific geometry were explored by time-dependent DFT (TDDFT) calculation in the Gaussian16 package at B3LYP/6-311G** level of theory. Mostly, the HOMO was localized at the DMA and LUMO was localized at pyrene, in both the systems (Figure 2b) (Table S4). This partially separated HOMO (-5.23eV in PyCHDMA1; -5.19eV in PyCHDMA20) and LUMO (-1.66eV in PyCHDMA1; -1.67eV in PyCHDMA20) indicates a charge transfer state property of both the systems (Table S6).[30] The formation of ICT states belonging to the LUMO←HOMO transition is consistent with the observed solvatochromism and large Stokes shifts.[27] The $S_1 \leftarrow S_0$ transition is mixed in nature and the LUMO←HOMO-1 which assigned as LE transition, contributes 90% in that (Table S7).

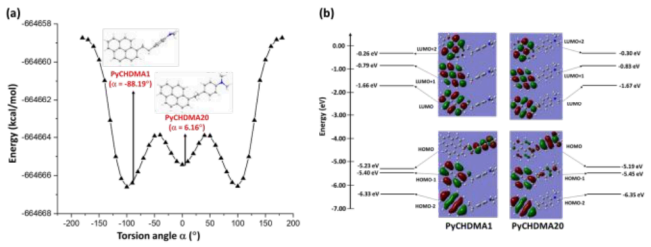

Figure 2. (a) PES plot for energy vs torsion angle. The molecular conformation of the single crystal structures is also shown on the plot. (b) Molecular orbitals obtained from TDDFT calculations for PyCHDMA1 and PyCHDMA20 are plotted with energy values.

The TDDFT results were further utilized in the analysis and visualization of the atom-to-atom and inter-fragment charge transfer during $S_1 \leftarrow S_0$ excitation, as heat maps, known as charge transfer matrix (CTM).[31] The CTMs were plotted, to quantitatively analyze the inter- and intra-fragment charge transfer, via the inter-fragment charge transfer (IFCT) method incorporated in the Multiwfn 3.6 program.[31] In the present study, the hole and

electron distributions were calculated with the IFCT method by employing the Hirshfeld partition. The inter-and intra-fragment electron transfer was studied by dividing the entire molecule into three fragments for both the polymorphs. The three fragments for both the polymorphs are pyrene, DMA, and the alkane linker $(CH_2)_2$. The contributions of various fragments to holes and electrons, for $S_1 \leftarrow S_0$ transitions are also presented (Table S8). For the single electron excitation, the results show that the electron on the DMA moiety is reduced by 0.9510 during the electron excitation process, while the pyrene moiety has gained 0.9626 electrons. Quite similarly, for PyCHDMA20 fragment 1 i.e. DMA moiety lost 0.8527 electrons and pyrene moiety gained 0.8701 electrons, during the $S_1 \leftarrow S_0$ excitation process. Figures 3a and b show the charge transfer matrix (CTM) diagram for PyCHDMA1 and PyCHDMA20, respectively, which exhibit the atom-to-atom charge transfer. Both the CTMs suggest that atom no. 1 (nitrogen) in the DMA moiety is transferring most electrons to atom no. 10, 12, 17, and 19, in the pyrene moiety. Figure 3b also exhibits that the redistribution of electrons within pyrene moiety is more for PyCHDMA20 compared to PyCHDMA1, as suggested by a brighter region on the CTM, highlighted with a red square (Table S9). Figures 3c and d show the numbering of the atoms and the fragments for the purpose of the present analysis. Figures 3e and f show the CTM diagram plotted based on fragments, for PyCHDMA1 and PyCHDMA20. These CTMs as well as the values presented in Table S10, for both the polymorphs suggest that electron transfer is mostly happening from fragment 1 to fragment 3, for the $S_1 \leftarrow S_0$ excitation. While fragment 1 is the DMA moiety and fragment 3 is the pyrene moiety. The linker group, $(CH_2)_2$ has very little contribution in the electron transfer from fragment 1 to fragment 3.

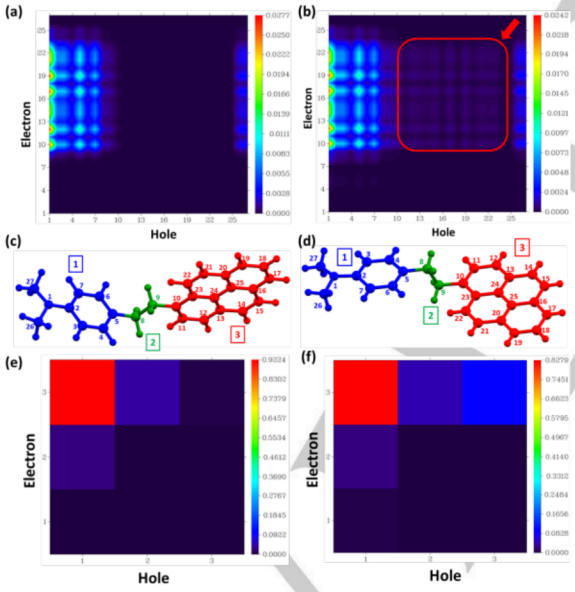

Figure 3. The atom-to-atom charge transfer matrix (CTM) of (a) PyCHDMA1 and (b) PyCHDMA20, for $S_1 \leftarrow S_0$ excitation are presented as heat maps. Numbering of atoms and fragments in (c) PyCHDMA1 and (d) PyCHDMA20. The inter-fragment charge transfer matrix (CTM) of (e) PyCHDMA1 and (f) PyCHDMA20, for $S_1 \leftarrow S_0$ excitation are showed as heat maps.

In order to understand the structural changes in the event of ICT, the ground state (GS) and 1st excited state (ES) geometries of both the systems are optimized at B3LYP/6-311G** level of theory. The major difference observed between the GS and 1st ES optimized geometry could be reflected in the movement of the tertiary N atom in the DMA moiety which involves N1 going into the plane containing C2, C26, and C27 atoms and the shortening of the N1-C2 bond. The pyramidalization of the tertiary amine in the DMA moiety is due to the presence of lone pair on the N atom, which heavily contributes to the ICT, as exhibited earlier with IFCT methods for $S_1 \leftarrow S_0$ excitation. As a result, the pyramidalization goes down in the CT state. The decrement in the pyramidalization was observed for both the ES optimized geometries, in PyCHDMA1 (N atom moved into the plane by 0.171Å) is similar to PyCHDMA20 (N atom moved into the plane by 0.173Å) (Figure 3b, d).

Apart from the axial orientation of pyrene and DMA moieties, the other important difference between the PyCHDMA1 and PyCHDMA20 crystal structures was the extent of overlap between the π-π stacked pyrene moieties. Which is ~66% for PyCHDMA1 and ~17% for PyCHDMA20. Although the extent of overlap of effective van der Waals volume between the two π-π stacked molecules is more for PyCHDMA20 compared to PyCHDMA1 (Figure S16). The interaction energy between the π-π stacked dimers in PyCHDMA20 crystals is higher than PyCHDMA1, in GS, as suggested by the energy framework analysis performed with the CrystalExplorer program. The chance of dimerization of the π-π stacked molecules in both the crystals is quite high. The overall differences in the intermolecular interactions or stacking behavior are reflected in the TCSPC results while exciting the crystals with 375nm laser at 77K and 296K (Table S7). We have used a 468nm LP filter to get rid of any emission below that wavelength and since CT band or excimer bands was mostly appearing beyond that range even in the solution. For PyCHDMA20 crystals, going from 296K to 77K, there was no lifetime longer than 66ns for any species but for PyCHDMA1, at 77K a small population was observed with a lifetime of ~108ns. The comparatively longer lifetimes observed for both the crystals can be attributed to the excimer lifetime which has formed while exciting with 375nm radiation. The shorter lifetimes, ~3ns for PyCHDMA1 and ~7ns for PyCHDMA20, can be attributed to the emissive CT state. The intensity count of the emission maxima corresponds to ICT band reduced with lowering the temperature from 296K to 78K. The lifetimes of ICT states in crystals are in good agreement with earlier reported studies.[14][32] The excimer population for PyCHDMA20 goes significantly up going from 296K (18%) to 77K (43%).

Finally, the time-resolved photocrystallography measurements in the pink Laue regime shed light on the photo-induced structural changes in PyCHDMA1 and PyCHDMA20 crystals. The pink Laue pump-probe data sets were collected at a 15 keV (≈0.82656Å) undulator setting. In order to maximize the overlap between the pump and probe beam on crystals since the penetration of the laser beam inside the crystals is quite poor, the experimental geometry is set up in a way that the laser-pump beam was coming to crystals perpendicular to the X-ray probe beam (Figure S20). All the crystals were excited with 390 nm laser pulses and subsequently probed by the ≈100*ps* X-ray pulse with a pump−probe delay of 1ns and 2ns for the PyCHDMA1 and PyCHDMA20 datasets, respectively. The time-resolved photocrystallography datasets were processed by the RATIO method[33] (based on the intensity ratios, $R = I_{ON}/I_{OFF}$), incorporated in the LaueUtil toolkit[34]. For each set of goniometer angles, laser-ON and laser-OFF frames were collected in quick succession, at least 5 times each, to improve the statistics of the

experimental intensity ratios. For PyCHDMA1 (2 datasets) and PyCHDMA20 (3 datasets), multiple data sets were processed with the LAUEUTIL toolkit.

Before the beginning of collecting more extensive datasets we have collected a couple of short datasets with slightly varying laser powers. These power scans were measured in order to verify the existence of a photo-induced response in the crystals and also to check the reproducibility of the measurements.[35] The correlation between the ratio values measured in these power scans is quite reasonable, as shown in Figure S24.

The different datasets collected with different crystals were jointly refined against a common ES geometry. The ratio values, $R = I_{ON}/I_{OFF}$ obtained for these datasets are also showed satisfactory correlation as the ratio-correlation plot depicted in Figure S29. In joint refinement, the ES geometry of the molecules agrees well with all the datasets with their separate respective population and thermal scale parameters. Subsequently, a combined scaled-merged data set was obtained by scaling those well-correlated individual data sets by a scale factor $k(\eta)_{set} = \langle|\eta|\rangle_{all}/\langle|\eta|\rangle_{set}$; in which $\langle|\eta|\rangle_{all}$ is the average response ratio, defined as $\eta_{ON/OFF}(\mathbf{h}) = R_{ON/OFF}(\mathbf{h}) - 1$, overall measured reflections and $\langle|\eta|\rangle_{set}$ is the average over all the reflections measured in a particular dataset.[36] The combined scaled data sets were then merged using the SORTAV program.[37] The purpose of creating combined scaled-merged datasets from individuals is to have better completeness of the data necessary to plot various difference Fourier maps.[36]

A reliable way of illustrating the light-induced differences between laser-ON and laser-OFF electron density distribution is through plotting photodifference maps.[38] The photodifference maps obtained with combined scaled-merged datasets suggest that along with other atomic shifts, there was a shift of the tertiary nitrogen atom into the plane containing three carbon atoms bonded to it (Figures 4a and b). This was already observed in the theoretically optimized geometries with DFT methods, as discussed earlier.

The photodifference maps are quite useful, in helping one select parameter in intensity-ratio ($R = I_{ON}/I_{OFF}$)-based least-squares refinements with the LASER program.[39] The program LASER refines the atomic positions, excited state population (P), and temperature scale factor (k_B). The random distribution (RD) model was used in the refinement of ES species geometry in a crystal, in which the total calculated structure factor for the laser-ON structure is expressed as, $|F_c^{ON}| = P.|F_c^{ES}| + (1 - P).|F_c^{GS}|$; where P is the population factor of the species, and F_c^{ES} and F_c^{GS} are the ES and GS molecule structure factors, respectively. The random distribution (RD) model is based on a random distribution ES molecules in the crystal and works well when conversion percentages are quite low.[39a] Positions of the atoms belonging to the DMA and connecting CH_2-CH_2 groups were freely refined, whereas the entire pyrene moiety was treated as a rigid body anchored on a carbon atom.

Thermal motion increase was modeled by introducing the temperature scale factor (k_B), which relates the U_{ij}'s of the laser-ON and laser-OFF structures in the following way: $U_{ij}^{ON} = k_B . U_{ij}^{OFF}$. The k_B values obtained from LASER refinement results are not far off from the values obtained from the slope of the photo-Wilson plots[40] for both the conformers (Table 1).

For PyCHDMA1, the excited state (ES) population of the two datasets is 1.30% and 1.05%. Whereas, for PyCHDMA20, the ES population ranges from 0.89% to 1.59% (Table 1). The relatively low population ES species and small increment of the B factor can be attributed to the fact, that the operating power of the pump laser was kept to a level at which a sufficient amount of data could be collected without damaging the crystal, and probably a low quantum efficiency at 100K as suggested by the reduction in the emission maxima corresponding to ICT band with lowering the temperature, suggested elsewhere too.[28a] It was also important to have the same unit cell dimensions for both laser-OFF and laser-ON frames in order to use the RATIO method successfully. The refined excited state geometry shows along with the deduction of the bond length for N1-C2, that there are other bond lengths in the DMA moiety that have reduced in length. The result of intramolecular electron transfer in ES is quite clear in the form of shortening of the N-C bond and a reduction in the pyramidalization at the C-N-$(CH_3)_2$ moiety within DMA by 0.114Å and 0.087Å in PyCHDMA1 and PyCHDMA20, respectively.

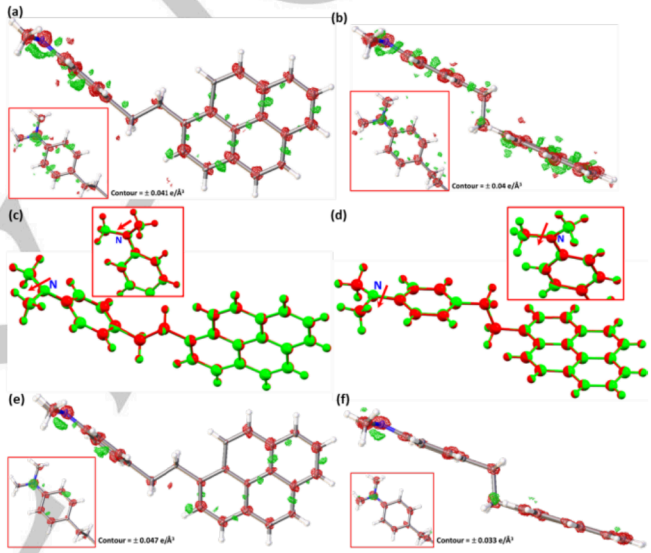

Figure 4. Photodifference maps of (a) PyCHDMA1 and (b) PyCHDMA20. Superposition of GS and ES refined geometries for (e) PyCHDMA1 and (f) PyCHDMA20. Green is for GS structure and red for ES structure. Contours of the maps are also indicated on the figures. Photodeformation maps of (c) PyCHDMA1 and (d) PyCHDMA20. Maps were drawn using the combined scaled-merged data sets.

The movement of atoms in ES geometry obtained from TRXRD measurements agrees well with the theoretically optimized geometries by DFT methods. Although the extent of atomic shifts is sometimes more drastic with the DFT optimized geometries. Especially, the movement of tertiary nitrogen into the plane containing three carbon atoms all bonded to it, is much more pronounced for the DFT optimized geometries. The atomic shifts observed in the 1st ES in the DFT optimized geometries for both the conformers are quite similar and in agreement with the results obtained from IFCT analysis, earlier.

Table 1. Data processing parameters, and population and temperature scale factors obtained from individual and combined datasets after LASER refinement.

Data sets	N_{ref}[a]	C(%)[b]	P(%)[c]	k_B	k_B from photo-Wilson plots

PyCHDMA1_1ns	1620	51.8	1.30(11)	1.055(2)	1.075
PyCHDMA1_1ns1	1310	42.1	1.05(8)	1.046(2)	1.065
PyCHDMA20_2ns	2396	38.2	1.59(12)	1.058(1)	1.072
PyCHDMA20_2ns1	1997	31.8	1.58(16)	1.042(2)	1.085
PyCHDMA20_2ns2	2184	34.8	0.89(10)	1.057(1)	1.054

[a] Number of reflections after merging in SORTAV. [b] Completeness of data. [c] Population of excited state species. The completeness for all the datasets were calculated at 0.59 Å^{-1} resolution.

Finally, the photo-deformation maps,[23b,38b] calculated using the LASER refined model parameters, that represent the difference between the densities calculated with the ES parameters and the GS structure, show a stronger atomic shift at the nitrogen atom position for both the conformers. The major reason for the stronger appearance of the nitrogen atom shifts reflected in the difference Fourier maps, be it photodifference or photodeformation can be attributed to the fact that not only does it have one more electron than the carbon atoms bonded to it but it also moves more in the ES than rest of them (Table S29).

In order to know the ICT interaction energies involving the DMA moiety, especially, the nitrogen atom, natural bond orbital (NBO)[41] analysis at M06-2X/6-311G** level of theory in the gas phase, using the GS and ES geometries, from X-ray diffraction studies and DFT optimization were utilized. The NBO analysis allowed us to calculate the donor-acceptor interaction energies involving the lone pair (LP) of nitrogen atom as the donor, from 2nd order perturbation theory analysis of Fock matrix in NBO basis, with E(2) ≥ 0.05kcal/mol as listed in Tables S11, S12, S13 and S14. The interaction energies provide a measure of the strength of the intramolecular charge transfer interaction. The reduced lone pair feature at the N atom of the DMA moiety in the ES geometry obtained from single crystal XRD studies for both the polymorphs is established using the NBO calculations.[42] Table 2 suggests an increased p character (ES: 99.34% in PyCHDMA1 and 98.98% in PyCHDMA20) of the lone-pair (LP) orbital in the ES for both the polymorphs, validating the prominent sp^2 character for the nitrogen atom in ES refined geometry. Furthermore, it shows a better overlap between LP and anti-bonding π* C–C orbitals (Figure S20). However, in both the conformers, NBO analysis of GS shows a relatively lesser overlap between LP and π* C–C orbitals compared to ES due to the mixture of s and p character in the LP of nitrogen. Stabilization energy (second-order perturbation energies E(2)) corresponding to the intramolecular charge transfer involving the LP of the nitrogen atom in ES is greater than GS for both the polymorphs. Therefore, as a result of larger intramolecular charge transfer in ES, the N-C bond gets shortened and the repulsion between the lone pair and the bond pair in the central nitrogen atom decreases inducing the planarity in the C-N-$(CH_3)_2$ moiety.

Table 2. The strongest intramolecular charge transfer interactions involving the donor LP orbital of nitrogen and acceptor π* C–C orbitals, in PyCHDMA1 and PyCHDMA20 geometries obtained from single crystal XRD studies, based on the 2nd order perturbation theory analysis of Fock matrix in NBO basis, along with the hybridization, are listed.

Donor NBO's (i)/ Hybridization	Acceptor NBO's (j)/ Hybridization	E(2) (kcal/ mol)	E(j) – E(i) (a.u.)	F(i, j) (a.u.)
PyCHDMA1 (GS)				
93. LP (1) N1 s (4.59%) p20.77 (95.39%) d0.00 (0.02%)	565. BD*(2) C2 – C10 (54.62%) C2 s(0.02%) p99.99(99.94%) d1.91(0.04%) (45.38%) C10 s(0.00%) p1.00(99.97%) d0.00(0.02%)	45.66	0.37	0.12
PyCHDMA1 (ES)				
93. LP (1) N1 s (0.65%) p99.99 (99.34%) d0.01 (0.01%)	571. BD*(2) C10 - C18 (56.30%) C10 s(0.36%) p99.99(99.60%) d0.09(0.03%) (43.70%) C18 s(0.80%) p99.99(99.18%) d0.02(0.02%)	63.65	0.33	0.14
PyCHDMA20 (GS)				
93. LP (1) N1 s (4.05%) p23.66 (95.93%) d0.00 (0.02%)	564. BD*(2) C2 - C3 (54.66%) C2 s(0.03%) p99.99(99.94%) d1.31(0.04%) (45.34%) C3 s(0.00%) p1.00(99.98%) d0.00(0.02%)	47.94	0.37	0.12
PyCHDMA20 (ES)				
93. LP (1) N1 s (1.03%) p96.39 (98.97%) d0.01 (0.01%)	571. BD*(2) C10 - C18 (54.91%) C10 s(0.01%) p1.00(99.95%) d0.00(0.04%) (45.09%) C18 s(0.00%) p1.00(99.97%) d0.00(0.03%)	55.34	0.36	0.13

[Note: E(*i*) corresponds to Lewis type "filled" donor orbitals. E(*j*) corresponds to non-Lewis type "unfilled" acceptor orbitals. BD = 2-center bond, BD* = 2-center anti-bonds.
For each donor NBO (*i*) and acceptor NBO (*j*), the stabilization energy *E*(2) associated with $i \rightarrow j$ delocalization is determined as,

$$E(2) = \Delta E_{ij}^{(2)} = \frac{q_i F(i,j)^2}{\varepsilon_j - \varepsilon_i}$$

Where, q_i: is the donor orbital occupancy.
ε_i, ε_j are diagonal elements (orbital energies) of NBO Fock matrix.
F(*i*,*j*) is the off-diagonal NBO Fock matrix elements.]

NBO analyses for the interaction energies between the π-π stacked dimers were also performed at M06-2X/6-311G** level of theory in the gas phase, using the GS and ES geometries obtained by X-ray diffraction studies and DFT optimizations.[43] There was no appreciable difference in the interaction energies involving the π-π stacked dimers between the GS and ES for both the polymorphs. The results prove that the intermolecular interactions between the π-π stacked dimers are not contributing much to the excited state charge transfer process (Table S15 and S16). Although the interaction energies suggest the formation of excimers in both the conformers at GS and ES.[42] The results from the output of NBO analysis in gaussian also provide the individual atomic charges calculated by natural population analysis (NPA) and Hirshfeld population analysis (HPA). Both the analysis shows that the negative charge on the nitrogen atom has reduced in the ES for both the polymorphs (Table S19 and S20).

Conclusion

The ICT molecule PyCHDMA was crystallized in two conformational polymorphic forms. The conformational difference between the conformers could be described by rotation about a single bond. While in PyCHDMA1, the electron donor DMA moiety and the electron acceptor pyrene moieties could be described as in axial orientation, in PyCHDMA20 they are in the equatorial position. The obvious conformational differences have prompted us to investigate the polymorphs from the perspective of

photoinduced ICT. The emission spectra of PyCHDMA in different solvents show a bathochromic shift of the CT band maxima with a gradual increment of polarity, suggesting the intramolecular nature of the charge transfer process. The TDDFT calculation for both the conformers shows that the HOMO and LUMO are spatially separated with HOMO entirely located on DMA moiety and the LUMO is on pyrene, indicating charge transfer nature for the LUMO←HOMO transition. The intra- and interfragment electron transfer calculation for $S_1 \leftarrow S_0$ excitation with IFCT method in Multiwfn show that the entire electron transfer process from DMA moiety to pyrene moiety is dominated by the transfer of electrons from nitrogen atom to pyrene moiety. The electron transfer in this case happens through tunneling. The linker $(CH_2)_2$ group does not contribute much to the electron transfer process and therefore does not get used as a hopping station during the electron transfer. The calculation also indicates the absence of the back-electron transfer process in both the conformers. In PyCHDMA20, IFCT analysis suggests more intrafragment electron reorganization within pyrene moiety for $S_1 \leftarrow S_0$ excitation.

The time-resolved photocrystallography measurements with the single crystals of these two conformational polymorphs have also shown a similar picture. The photo-induced changes in the molecular geometry in the single crystals of the conformers are also quite comparable. The population of the excited state species and the increment of temperature due to laser-induced processes are also not very different between the conformers. A significant amount of intramolecular electron transfer from the nitrogen atom in ES was identified with the shortening of N1-C2 bond and a reduction of pyramidalization at the nitrogen atom in the DMA moiety. The analysis of the hybridization at the nitrogen atom also showed that the LP of the nitrogen atom in ES is having a much purer p characteristic while in the case of GS, the LP of the N atom is characterized by a mixture of s and p character, with a more noticeable contribution for s character. The transfer of electrons from the nitrogen atom caused a decrement in the repulsion between the lone-pair and the bond pair in the central nitrogen atom which in turn induced planarity in the C-N-(CH3)2 moiety. The same feature of N1-C2 bond shortening and the planarity of the C-N-(CH3)2 moiety was also observed in the DFT optimized geometry belonging to 1st excited state, for both polymorphs.

The NBO analysis with the theoretically and experimentally obtained geometries in GS and ES portrays strong intramolecular charge-transfer interaction between the lone-pair (LP) orbital of the nitrogen with the π^* C–C antibonding orbital in both the polymorphs. The interaction energies from NBO analysis suggest an absence of charge transfer in the ES, between the π-π stacked dimers in both systems. Finally, the natural population analysis and Hirshfeld population analysis with both systems showed a significant amount of reduction in the atomic charge on the nitrogen atom, going from GS to ES.

The formation of conformational polymorphs for an ICT molecule like PyCHDMA, where the electron donor group DMA is linked to the electron acceptor group pyrene through a short alkane chain has provided a unique opportunity to investigate the intramolecular electron transfer process that can be externally stimulated by light photon. The advent of ultrafast lasers and detectors with fast read-out has facilitated the real-time investigation of the charge transfer processes, greatly, in both natural and synthetic systems. The studies on photoinduced charge transfer provide an excellent opportunity to prepare ourselves for the efficient use of sunlight. The process of solar energy conversion can be also quite useful in replacing our reliance on fossil fuel with an easily available, abundant, inexpensive, and eco-friendly renewable energy source.[44]

Experimental Section

All the relevant characterization data and figures are provided in the Supporting Information.

Acknowledgements

S.T. is grateful for financial support within the ECRAPS and FISCOV Innovation Funds of the Helmholtz Association (HGF). The CMWS-Early Science Program of DESY/HGF is also acknowledged (S.T.). Use of the Center for Nanoscale Materials, an Office of Science user facility, was supported by the U.S. Department of Energy, Office of Science, Office of Basic Energy Sciences, under Contract No. DE-AC02-06CH11357. We acknowledge DESY (Hamburg, Germany), a member of the Helmholtz Association HGF, for the provision of experimental facilities. A part of the research was carried out at the light source PETRA-III at DESY, a member of HGF. We would like to thank P11 staff for assistance. J.G.V., D.S., S.V.T. and S.T. acknowledge project B06 of the SFB1073 of the Deutsche Forschungsgemeinschaft (DFG, German Research Foundation) - 217133147/SFB 1073. K.B. acknowledges Dr. Sumit Naskar for the discussions on NBO analysis with DFT methods and IFCT analysis with Multiwfn. We hereby acknowledge that the synthesis has been performed in the largest amount at FS-SCS / DESY, and in small amounts at the Facility for Synthetic Chemistry at the Max-Planck Institute for Biophysical Chemistry.

Keywords: photoinduced electron transfer • Polymorphs • photocrystallography • charge transfer • Donor-bridge-acceptor system

[1] J. Deisenhofer, H. Michel, *Science* **1989**, *245*, 1463-1473.
[2] D. B. Hall, R. E. Holmlin J. K. Barton, *Nature* **1996**, *382*, 731–735.
[3] P. Song, Y. Li, F. Ma, T. Pullerits, M. Sun, *Chem. Rec.* **2016**, *16*, 734–753.
[4] K. Yea, Y. Lib, H. Yanga, M. Lia, Y. Huangb, S. Zhangc, H. Jia, *Appl. Catal. B* **2019**, *259*, 118085.
[5] O. Kruse, J. Rupprecht, J. H. Mussgnug, G. C. Dismukes, B. Hankamer, *Photochem. Photobiol. Sci.* **2005**, *4*, 957–969.
[6] a) Y. Xing, Y. Xu, Q. Wu, G. Wang, M. Zhu, *J. Mater. Chem. C* **2021**, *9*, 439-455; b) C.-F. Liu, H. Lin, S.-S. Li, H. Xie, J.-L. Zhang, D.-Z. Ji, Y. Yan, X. Liu, W.-Y. Lai, *Adv. Func. Mater.* **2022**, *32*, 2111276.
[7] S. Techert, A. Wiessner, S. Schmatz and H. Staerk, J. Phys. Chem. B, **2001**, *105*, 7579 – 7587.
[8] A. Nakajima, *Bull. Chem. Soc. Jpn.* **1973**, *46*, 2602−2604.
[9] a) S. Techert, S. Schmatz, A. Wiessner, H. Staerk, *J. Phys. Chem. A* **2000**, *104*, 5700-5710; b) A. Ramos, S. Techert, *Biophys. J.* **2005**, *89*, 1990 – 2003; c) S. Thekku Veedu, D. Raiser, R. Kia, M. Scholz, S. Techert, *J. Phys. Chem. B* **2014**, *118*, 3291−3297.
[10] a) T. Okada, M. Migita, N. Mataga, Y. Sakata, S. Misumi, *J. Am. Chem. Soc.* **1981**, *103*, 4715-4720; b) N. Mataga, H. Chosrowjan, S. Taniguchi, *J. Photochem. Photobiol. C* **2005**, *6*, 37–79.
[11] a) Y. Yuan, X.-S. Yan, X.-R. Li, J.-L. Cao, Z. Li, Y.-B. Jiang, *Chem. Commun.* **2017**, *53*, 13137–13140; b) S. Mondal, D. N. Nath, *Spectrochim. Acta A* **2020**, *230*, 118019; c)

[12] T. M. Figueira-Duarte, K. Müllen, *Chem. Rev.* **2011**, *111*, 7260–7314.
[13] Z. Chu, M. Yang, P. Schulz, D. Wu, X. Ma, E. Seifert, L. Sun, X. Li, K. Zhu, K. Lai, *Nat. Commun.* **2017**, *8,* 2230.
[14] S. Techert, K. A. Zachariasse, *J. Am. Chem. Soc.* **2004**, *126*, 5593–5600.
[15] Z. R. Grabowski, K. Rotkiewicz, W. Rettig, *Chem. Rev.* **2003**, *103*, 3899–4031.
[16] a) W. Rettig, W. Majenz, *Chem. Phys. Lett.* **1989**, *154*, 335-341; b) R. Lapouyade, A. Kuhn, J.-F. Letard, W. Rettig, *Chem. Phys. Lett.* **1993**, *208*, 48-58.
[17] a) K. A. Zachariasse, M. Grobys, Th. Von der Haar, A. Hebecker, Y. V. Il'ichev, O. Morawski, I. Rückert, W. Kühnle, *J. Photochem. Photobiol A: Chem.* **1997**, *105*, 373; b) K. A. Zachariasse, *Chem. Phys. Lett.* **2000**, *320*, 8–13.
[18] A. J. Cruz-Cabeza, J. Bernstein, *Chem. Rev.* **2014**, *114*, 2170–2191.
[19] a) M. D. Cohen, G. M. J. Schmidt, *J. Chem. Soc.* **1964**, 1996–2000; b) M. D. Cohen, G. M. J. Schmidt, F. I. Sonntag, *J. Chem. Soc.* **1964**, 2000–2013; c) G. M. J. Schmidt, *Pure Appl. Chem.* **1971**, *27*, 647; d) A. Ravi, S. Z. Hassan, S. Bhandary, K. M. Sureshan, *Angew. Chem. Int. Ed.* **2022**, *61*, e202200954.
[20] a) S. Techert, F. Schotte, M. Wulff, *Phys. Rev. Lett.* **2001**, *86*, 2030–2033; b) C. D. Kim, S. Pillet, G. Wu, W. K. Fullagar, P. Coppens, *Acta Cryst.* **2002**, *A58*, 133–137; c) P. Coppens, *Angew. Chem. Int. Ed.* **2009**, *48*, 4280–4281; d) P. Coppens, *J. Phys. Chem. Lett.* **2011**, *2*, 616–621; e) L. E. Hatcher, P. R. Raithby, *Coord. Chem. Rev.* **2014**, 277–278, 69–79.
[21] a) H. Cailleau, M. Lorenc, L. Guerin, M. Servol, E. Collet, M. B.-L. Cointe *Acta Cryst.* **2010**, *A66*, 189–197; b) R. Bertoni, M. Cammarata, M. Lorenc, S. F. Matar, J.-F. Létard, H. T. Lemke, E. Collet, *Acc. Chem. Res.* **2015**, *48*, 774–781; c) J. D. J. Velazquez-Garcia, K. Basuroy, D. Storozhuk, J. Wong, S. Demeshko, F. Meyer, R. Henning, S. Techert, *Dalton Trans.* **2022**, *51*, 6036-6045.
[22] K. Basuroy, Y. Chen, S. Sarkar, J. Benedict, P. Coppens, *Struct. Dyn.*,**2017**, *4*, 024501 – 024509.
[23] a) A. Makal, J. Benedict, E. Trzop, J. Sokolow, B. Fournier, Y. Chen, J. A. Kalinowski, T. Graber, R. Henning, P. Coppens, *J. Phys. Chem. A* **2012**, *116*, 3359–3365; b) K. N. Jarzembska, R. Kaminski, B. Fournier, E. Trzop, J. Sokolow, R. Henning, Y. Chen, P. Coppens, *Inorg. Chem.* **2014**, *53*, 10594–10601.
[24] E. Collet, M.-H. Lemée-Cailleau, M. B.-L. Cointe, H. Cailleau, M. Wulff, T. Luty, S.-Y. Koshihara, M. Meyer, L. Toupet, P. Rabiller, S. Techert, *Science* **2003**, *300*, 612-615
[25] Y. H. Zhao, M. H. Abraham, A. M. Zissimos, *J. Org. Chem.* **2003**, *68*, 7368-7373.
[26] P. R Spackman, M. J. Turner, J. J. McKinnon, S. K. Wolff, D. J. Grimwood, D. Jayatilaka, M. A. Spackman, *J. Appl. Crystallogr.* **2021**, *54*, 1006–1011.
[27] X. Zhang, J. Wang, Y. Liu, Y. Hao, F. Yu, D. Li, X. Huang, L. Yu, T. Wang, H. Hao, *J. Phys. Chem. C* **2021**, *125*, 6189−6199.
[28] Y. Zhao, D. G. Truhlar, *Theor. Chem. Acc.* **2008**, *120*, 215 – 241.
[29] B. K. Hodnett, V. Verma, *Processes* **2019**, *7*, 272–283.
[30] K. Wang, Y. Xie, M. Liu, W. Tao, H. Zhang, M. Huang, J. You, Y. Liu, Y. Li, Z. Li, Y. Q. Dong, *Adv. Optical Mater.* **2020**, 8, 2000436.
[31] a) T. Lu, F. Chen, *J. Comput. Chem.* **2012**, *33*, 580–592; b) T. Lu, *Multiwfn Manual*, *version 3.6(dev), section 3.21.1 and 3.21.8,* available at http://sobereva.com/multiwfn.
[32] S. I. Druzhinin, A. Demeter, K. A. Zachariasse, *Chem. Phys. Lett.* **2001**, 347, 421-428.
[33] P. Coppens, M. Pitak, M. Gembicky, M. Messerschmidt, S. Scheins, J. Benedict, S.-I. Adachi, T. Sato, S. Nozawa, K. Ichiyanagi, M. Cholletd, S.-Y. Koshihara, *J. Synchrotron Rad.* **2009**. *16*, 226–230.
[34] a) J. Kalinowski, A. Makal, P. Coppens, *J. Appl. Crystallogr.* **2011**, *44*, 1182–1189. b) J. Kalinowski, B. Fournier, A. Makal, P. Coppens, *J. Synchrotron Radiat.* **2012**, *19*, 637–646.
[35] P. Coppens, A. Makal, B. Fournier, K. N. Jarzembska, R. Kaminski, K. Basuroy, E. Trzop, *Acta Crystallogr.* **2017**, *B73*, 23–26.
[36] A. Makal, E. Trzop, J. Sokolow, J. Kalinowski, J. Benedict, P. Coppens, *Acta Crystallogr.* **2011**, *A67*, 319–326.
[37] a) R. H. Blessing, *Crystallogr. Rev.* **1987**, *1*, 3–58. b) R. H. Blessing, *Acta Crystallogr.* **1995**, *A51*, 33–38. c) R. H. Blessing, *J. Appl. Crystallogr.* **1997**, *30*, 421–426.
[38] a) M. D. Carducci, M. R. Pressprich, P. Coppens, *J. Am. Chem. Soc.* **1997**, *119*, 2669-2678; b) B. Fournier, P. Coppens, *Acta Crystallogr.* **2014**, *A70*, 291–299.
[39] a) I. Vorontsov, P. Coppens, *J. Synchrotron Radiat.* **2005**, *12*, 488–493. b) I. Vorontsov, S. Pillet, R. Kaminski, M. S. Schmøkel, P Coppens, *J. Appl. Crystallogr.* **2010**, *43*, 1129–1130.
[40] M. S. Schmøkel, R. Kamiński, J. B. Benedict, P. Coppens, Acta Crystallogr. **2010**, *A66*, 632-636.
[41] E. D. Glendening, C. R. Landis, F. Weinhold, *WIREs Comput. Mol. Sci.* **2012**, *2*, 1–42.
[42] A. E. Reed, L. A. Curtiss, F. Weinhold, *Chem. Rev.* **1988**, *88*, 899–926.
[43] K. Basuroy, J. D. J. Velazquez-Garcia, D. Storozhuk, D. J. Gosztola, S. Thekku Veedu, S. Techert, *J. Chem. Phys.* **2021**, *155*, 234304.
[44] M. E. El-Khoulya, E. El-Mohsnawy, S. Fukuzumi, *J. Photochem. Photobiol. C* **2017**, *31*, 36-83.